CFD analysis of gas flow through corrugated sheet structured packing: effects of packing geometry

Martin Isoz[*,†,‡] and Jan Haidl[¶]

Institute of Thermomechanics of the Czech Academy of Sciences, Prague, Department of Mathematics, University of Chemistry and Technology, Prague, and Department of Chemical Engineering, University of Chemistry and Technology, Prague

E-mail: isozm@it.cas.cz

Abstract

To accelerate the design of separation columns, packing vendors seek a reliable model of the flow in the complex geometry of the separation column packing. We provide a CFD model for the gas flow through various types of structured packings consisting of corrugated sheets. The model is validated on experimental data measured on commercial structured packings Mellapak 250.X, 250.Y, 350.Y and 500.Y. Furthermore, the measurements on Mellapak 250.X and 250.Y were performed with three different gases, He, N_2 and SF_6, to cover the widest possible range of operating conditions. A successfully validated model was used to estimate the dry pressure loss in relation to the gas flow and selected geometric parameters of the packing. The modified geometric

[*]To whom correspondence should be addressed

[†]Institute of Thermomechanics of the Czech Academy of Sciences, Dolejskova 5, 182 00 Prague, Czech Republic

[‡]Department of Mathematics, University of Chemistry and Technology, Studentska 5, 166 28 Prague, Czech Republic

[¶]Department of Chemical Engineering, University of Chemistry and Technology, Prague

parameters were specifically (i) the slope of the packing channels to the horizontal plane, (ii) the specific area of the packing, and (iii) the packing perforation density.

Nomenclature

Geometry parameters

a_{ch}[m] ..... length of packing channel side

a_{G}[m^{2}m^{-3}] ..... packing geometric area density

a_{pr}[m] .. distance between two perforation holes

B ..... packed bed geometry

D_{pr}[m] ..... perforation hole diameter

D_{pk}[m] ..... packing diameter

H_{pk}[m] ..... packing element height

N_{ch}[1] ..... number of channels in packing sheet

N_{pk}[1] ... number of packing elements in packed bed

N_{sh}[1] .... number of sheets in packing element

(O, x, y, z) ..... global coordinate system

$(\tilde{O}_i, \tilde{x}_i, \tilde{y}_i, \tilde{z}_i)$ ..... i-th local coordinate system

P_i ..... i-th packing element geometry

s_{ch}[m] ..... side of packing channel

S_i ..... i-th corrugated sheet geometry

w_{sh}[m] ..... width of the metal sheet

α_{ch}[1] ..... channel inclination angle

$\varepsilon_{\mathrm{pk}}$[1] ..... packing mean porosity

θ_{ch}[1] ..... angle between packing channel sides

φ_{pk}[1] ..... angle between two packing elements

Model variables and parameters

d_h[m] ..... channel hydraulic diameter

Δp_h[Pa m^{-1}] ..... packing dry pressure loss

$(\Delta p_h)_n$ [1] ..... normalized dry pressure loss

k[m^{2}s^{-2} ..... turbulence kinetic energy

I_0[1] estimate of in-channel turbulence intensity

p[m^{2}s^{-2}] ..... gas kinematic pressure

$(p)_n$ [1] ..... normalized pressure

$\boldsymbol{\tau}$[m^{2}s^{-2}] ..... stress tensor

u_i[m s^{-1}] ..... gas inlet velocity

u_f[m s^{-1}] .. estimate of gas free stream velocity

$\boldsymbol{u}$[m s^{-1}] ..... gas velocity

ν[m^{2}s^{-1}] ..... gas kinematic viscosity

Re[1] ..... gas flow Reynolds number

ρ[kg m^{-3}] ..... gas density

$\boldsymbol{\Phi}$[m s^{-1}] ..... flow direction with respect to $\partial\mathcal{S}$

ω[s^{-1}] ..... specific dissipation rate

Other symbols

$\mathcal{E}_A$ ..... absolute error

$\mathcal{E}_R$ ..... relative error

L_i ..... i-th mesh refinement level

$\mathbf{n}_f$. outer unit normal to the domain boundary

$\mathcal{S}$ ..... computational domain

$\partial\mathcal{S}$ ..... computational domain boundary

Introduction

The U.S. Department of Energy estimates that distillation columns are responsible for approximately 40% of the total energy consumption of the U.S.'s chemical industry.[1,2] Also, based on the recent energy consumption report in the European Union,[3] the chemical industry contributed 5% to total energy consumption in the European Union in 2014. Given that the structure of the chemical industry in the European Union and the United States is broadly similar, it can be estimated that the distillation columns in 2014 used up around 2% of total energy consumption across the European Union. In absolute values, this roughly corresponds to 32 million tonnes of oil equivalent (or $372 \cdot 10^6$ MWh) per year.[3]

Despite the energy-intensity of distillation, the design of the separation columns is still mostly empirical.[4,5] On the other hand, modest progress in construction or operation would result in substantial cost savings. Improvements in the design of the distillation columns are therefore currently considered to be the greatest opportunity to increase the efficiency and sustainability of the European chemical industry.[6]

One of the reasons of the current state of the distillation column design is the shear complexity of the technology involved. For example, due to the intricacies of the separations columns internals, it is almost impossible to reliably estimate the hydrodynamic properties of these devices without prior empirical experience. Furthermore, the modeling of the foretold phenomenon has long been constrained by the lack of both the necessary computing power and the appropriate models.

With the increase in available computational resources, the methods of computational fluid dynamics (CFD), particularly in the case of a single phase flow, can be used directly to resolve the flow across the whole column at once. This development has inspired a number of studies in this area. An extensive review of the CFD methods available for the design of packed absorption columns was given by Haroun and Raynal[7]. In addition, Owens et al.[8] developed an approach to modeling the gas flow through widely used structured packing, Mellapak 250.Y and they were able to estimate the packing dry pressure loss within 10%

difference from the experimental data. Owens et al.[8] proposed the use of X-ray computed tomography (CT) to generate model geometry. Such construction of the model requires the availability of a manufactured packing and a CT machine. However, the rest of the modeling process is automatic and the results can be obtained within hours. Amini et al.[9] used the CFD model to complete experimental performance evaluation of a new type of the structured packing and to speed up the packing design process. However, in this case CFD estimates for packing dry pressure loss differed by up to 50% from the experimental data.

Another notable result in CFD simulation of separation columns was achieved by Fernandes et al.[10],[11] who studied both dry and wet pressure loss in a structured packing. In particular, they focused on the Sulzer EX gauze structured packing and on the conditions corresponding to the supercritical fluid extraction. Both dry and wet pressure loss models were validated on the basis of available literature data. While the simulations for dry packing provided sufficient consistency with literature data (RSD of about 6%), simulated wet pressure losses varied from experimental values up to 30%.

Along with the studies carried out on the entire geometry of separation columns, there exists a significant number of results calculated on so called representative elementary units (REUs). Structured packings are highly regular structures. Raynal and Royon-Lebeaud[12] leveraged the regularity of the structured packings and proposed an approach based on a segmentation of the problems into three ranges of spatial scales: (i) the micro-scale REU to be solved directly via a full CFD model, (ii) the meso-scale corresponding to one element of the packing material, and (iii) the macro-scale that matches the entire column. The idea of Raynal and Royon-Lebeaud's approach is to solve exactly only a small part of the complex geometry involved, i.e. the REU, and to use the obtained information to construct an approximate model of larger spatial scales. Such an approach is a computationally less demanding process than CFD simulation of the whole macro-scale column. Hence, it enables detailed studies of the multiphase flow[13–17] coupled with heat and mass transfer.[18–20] Furthermore, Larachi et al.[21] used different REUs that matched the various geometric situ-

ations in column filled with structured packings to identify the contribution of the different dissipation mechanisms to the dry pressure loss of the whole packed bed.

In this paper, we provide a CFD model for gas flow in a widely used type of commercial packings, structured packing composed of corrugated sheets. Our main goal is to evaluate the effect of different packing geometry parameters on the dry pressure loss. The influence of the following geometric parameters of the packing is evaluated, (i) the channel inclination to the horizontal α_{ch}, (ii) the geometric area density of the packing a_{G}, and (iii) the packing perforation density expressed via the distance between the centers of two adjacent perforation holes a_{pr}.

Our overall approach used for the simulation construction was similar to the work of Owens et al. [8] with turbulence modeling based on the results of Khosravi-Nikou and Eshani [22]. However, due to the need to carry out a large number of simulations with different packing geometries, emphasis was put on the automation of the entire simulation process, including the packed bed geometry generation.

Geometry of the packed bed was prepared in Blender, [23] an open-source 3D creation suite. The simulations were performed using standard solvers available in OpenFOAM, [24] which is an open-source C++ library primarily focused on computational continuum mechanics and finite volume method (FVM). By combining Blender and OpenFOAM, we were able to generate the structured packing geometry and the corresponding mesh automatically. In addition, all operations connected to the model evaluation in the OpenFOAM software can be easily automated. Consequently, the presented model is suitable for parametric studies of the packing properties and for packing design.

We begin with a description of the experimental set up and the procedure used to validate the proposed model. Validation of the model was performed by comparing the estimated and measured dry pressure loss. The tested packings were Mellapak 250.X, 250.Y, 350.Y and 500.Y. To provide the model validation for a wide range of possible operating conditions, we performed the measurements of the dry pressure loss on Mellapak 250.X and 250.Y not only

with air/nitrogen but also with helium and sulfur hexafluoride. Due to the use of the two latter gases, the model validation data set included dry pressure losses measured for the gas Reynolds number in the range of about 100 to 10000.

The rest of the paper is devoted to the description of the CFD model and presentation of simulation results. First, we verify the proposed model against experimental data. Then, we comment on the minimum number of packing elements that are necessary to predict the dry pressure loss of the packed bed. Finally, the verified model is used to study the dependence of the packing dry pressure loss on the three aforementioned packing geometry parameters.

Experimental

The experimental pressure loss data of Mellapak 250.X (M250X), 250.Y (M250Y), 350.Y (M350Y) and 500.Y (M500Y) stainless steel structured packings have been measured in a 150.6 mm i.d. absorption column. The details of the used packings are given in Table 1. The packed bed consisted of six elements of packing; the individual packing elements were rotated around vertical axis by 90 degrees with respect to each other. The packed bed was installed 0.4 m above the mixing drum providing the calming section for the gas entering the packing, see Figure 1-(a).

Table 1: Details of the used packings. By a_{G}, we mark the packing geometric area density, a_{ch} and s_{ch} are the dimensions of a single packing channel as defined in Figure 1-(g), d_h denotes the hydraulic diameter of the channel and H_{pk} is the height of one packing element.

Packing	a_{G} [$\mathrm{m^2m^{-3}}$]	α_{ch} [1]	a_{ch} [mm]	s_{ch} [mm]	d_h [mm]	H_{pk} [cm]
M250X	250	60°	16.6	22.0	9.51	22.0
M250Y	250	45°	16.6	22.0	9.51	21.0
M350Y	350	45°	11.7	16.3	6.89	21.0
M500Y	500	45°	8.0	10.0	4.81	22.0

Four gases: air, nitrogen, helium and sulfur hexafluoride - were used during the measurements. The complete list of tested packings and experimental conditions is given in Table 2. The gas was circulated in a closed loop by means of a high speed fan. The gas flow rate

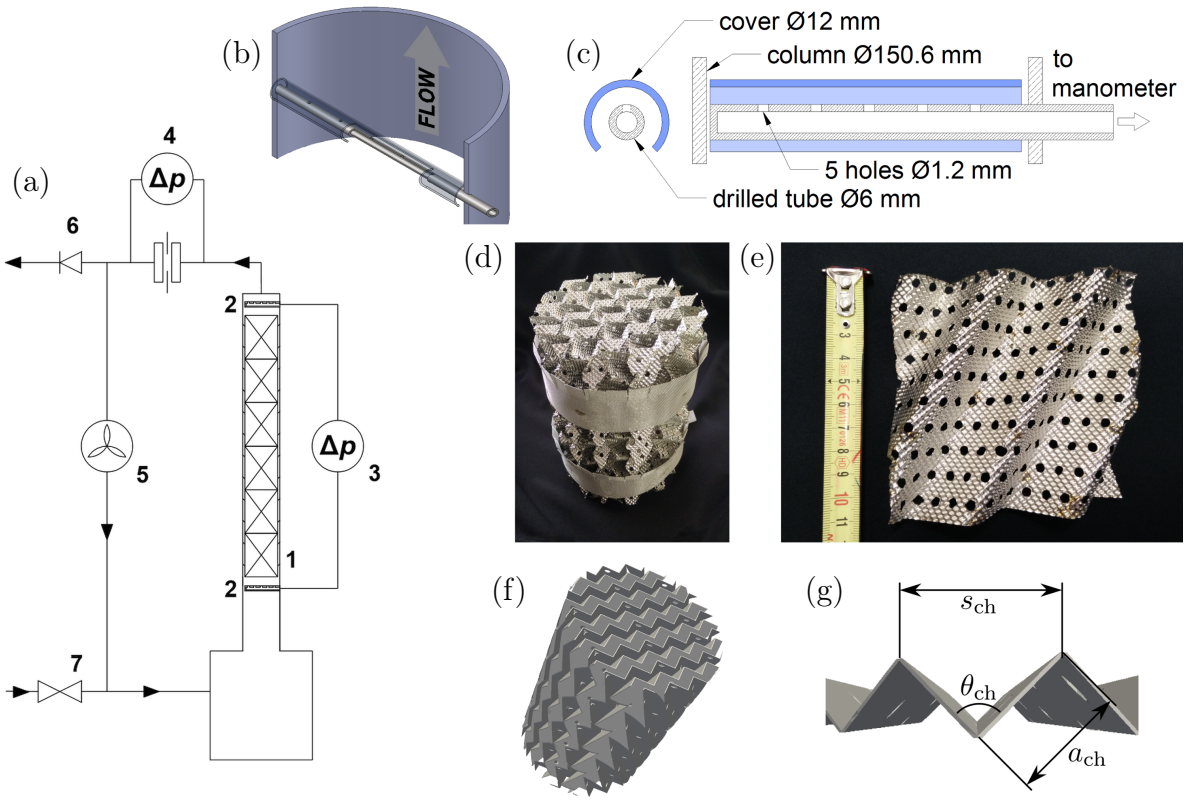

Figure 1: (a) Sketch of an experimental set-up. 1 - column with packed bed; 2 - pressure taps; 3 - ethanol manometer with inclined arm; 4 - calibrated orifice with differential pressure transducer; 5 - high speed fan; 6 - vent; 7 - pure gas make-up. (b) 3D model of the used pressure tap. (c) Sketch of the pressure tap. (d) Example of a separation column packing consisting of corrugated metal sheets. (e) Detail of one element of a dismantled packing. (f) Model geometry of one packing element of the Mellapak 250.X packing. (g) Detail of one packing channel.

was controlled via the fan revolutions and measured via the pressure loss across a calibrated orifice. The range of flow rates was limited from below by the sensitivity of the pressure transducer on the orifice and from above by the fan output.

In the case of measurement with pure gases, the column was operated at 200 Pa gauge pressure to prevent ambient air from being sucked in. Further, the content of the loop was continuously purged with small amount of pure gas from pressure cylinder to ensure high purity of the gas inside the loop. Assuming air to be the only gas penetrating into the loop, its concentration inside the loop was continuously monitored as an oxygen level by means of an oxygen optical probe. The concentration of air was kept below 3% during all the measurements. The density of the gas used for the evaluation of the measured data has been corrected for the presence of air.

Table 2: Overview of experimental conditions used during the pressure loss measurements.

Gas	$\rho\,[\mathrm{kg\,m^{-3}}]$	$\nu\,[\mathrm{m^2\,s^{-1}}]$	Packing	$u_{\min}\,[\mathrm{m\,s^{-1}}]$	$u_{\max}\,[\mathrm{m\,s^{-1}}]$
air	1.16	$15.5 \cdot 10^{-6}$	M350Y	0.49	4.07
			M500Y	1.08	2.93
nitrogen	1.15	$15.2 \cdot 10^{-6}$	M250X	0.46	4.31
			M250Y	0.83	4.28
helium	0.191	$105 \cdot 10^{-6}$	M250X	1.05	6.81
			M250Y	1.47	6.13
sulfur hexafluoride	5.71	$2.72 \cdot 10^{-6}$	M250Y	0.28	1.94

The pressure loss over the packing was measured as the pressure difference between two pressure taps placed approximately 5 cm below and above the packing, respectively. The pressure taps consisted of 15 cm long tubes drilled with five equally spaced 1.2 mm holes and connected to the ethanol manometer with an inclined arm, cf. Figure 1-(b) and (c). Before each set of measurements, i.e. for each packing and carrier gas, both the lines connecting the pressure taps and manometer have been purged with the gas from the column to prevent the potential error due to the different density of gas inside the column and connecting lines.

The zero level in the manometer has been adjusted separately for each measured dataset.

The combined uncertainties of the measured values have been estimated with respect to all the potential error sources, for all the experimental conditions and tested packings. For the gas flow rate, the combined uncertainty (σ_{u_i}) consists mainly from the uncertainties of calibration (3%) and of the pressure difference on the orifice (5 Pa). Hence, σ_{u_i} is approximately 3% of the maximal and 10% of the minimal used flow rate. The uncertainty of pressure loss measurement ($\sigma_{\Delta p_h}$) consists of the uncertainty of reading (1.6 Pa), uncertainty due to the oscillations (1%) and uncertainty due to the possible penetration of the air into the lines connecting manometer with the column. The maximal concentration of the air in the lines connecting the manometer with the column was assumed to be 10%. The resulting uncertainty due to the air penetration into the lines was 1 Pa for measurements with helium and 5 Pa for measurements with sulfur hexafluoride.

Computational domain and meshing

The structured packings consisting of corrugated sheets are geometrically highly complex structures, consult Figure 1-(d) and (e). The packing geometry was prepared automatically within the Blender software suite. The complete description of the automatic geometry generation is given in Algorithm 1 in Appendix. One example of a whole geometry of one packing element with a diameter $D_{\mathrm{pk}} = 0.14\,\mathrm{m}$ and height $H_{\mathrm{pk}} = 0.21\,\mathrm{m}$ is in Figure 1-(f).

The outputs of the Algorithm 1 were imported into the OpenFOAM meshing tool, the snappyHexMesh. The snappyHexMesh utility generates three-dimensional meshes containing hexahedra (hex) and split-hexahedra (split-hex) automatically from triangulated surface geometries.[24] As a core part of the OpenFOAM software, the snappyHexMesh is specialized on FVM calculations.

The mesh approximately conforms to the surface by iteratively refining starting mesh and morphing the resulting split-hex mesh to the surface.[24] The mesh quality is repetitively

controlled and adjusted during the meshing process, which enables the snappyHexMesh to provide high quality meshes even for complex geometries such as the studied Mellapak type packing. Furthermore, the utility is suitable for parallelization, scales well even on hundreds of cores[25] and thus it is applicable even to industrial size problems.

Due to the need to adjust the mesh to the complex geometry, the resulting mesh is unstructured. More specifically, if we denote the cells of the base mesh as the cells with the refinement level L_0, all the cells within 4 mm away from the geometry walls, i.e. from the column hull and the packing itself, are refined to the level L_1, where the refinement by one level corresponds to a splitting of the original cell to 8 approximately equivalent sub-cells. Moreover, all the cells within the distance 2 mm from the packing are refined to the level L_2. For the studied case of the packing diameter $D_{\mathrm{pk}} = 0.14\,\mathrm{m}$ and one packing element height $H_{\mathrm{pk}} = 0.21\,\mathrm{m}$, the resulting mesh size was of the order of millions cells per one packing element.

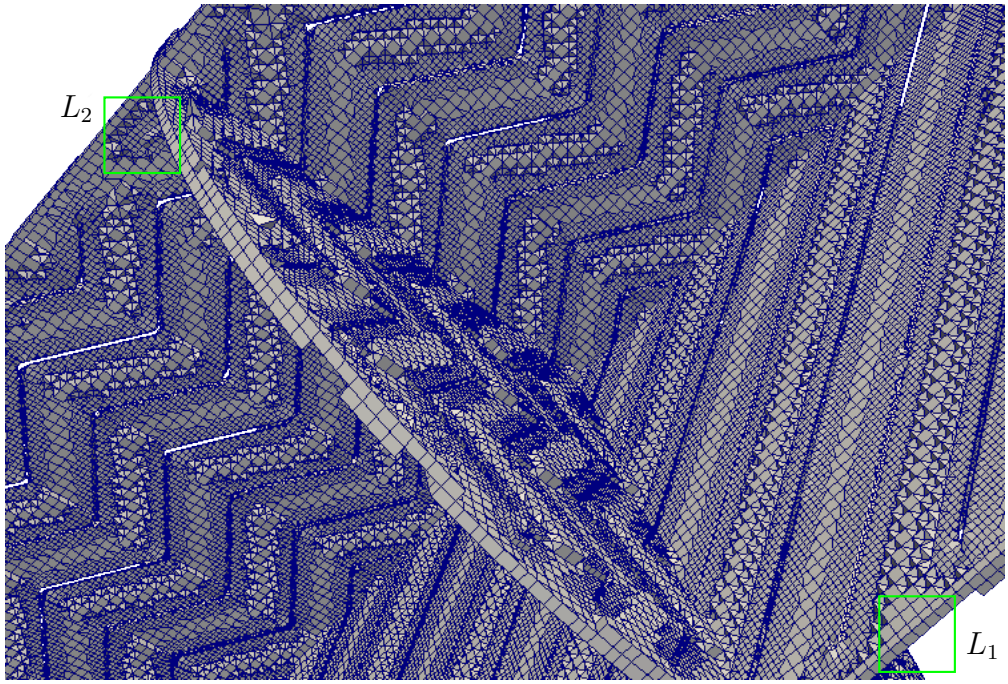

Figure 2: Mesh created for the Mellapak 250.Y packing. The depicted mesh has approximately $5.3 \cdot 10^6$ cells per one packing element. The cells with non-empty intersection with at least one of the planes $x = 0$, $y = 0$ and $z = 0$ are shown. Examples of L_1 and L_2 mesh refinement levels are highlighted. L_0 refinement level is not visible in the figure.

An example of the constructed mesh is depicted in Figure 2. The mesh refinement in the vicinity of the geometry walls is well visible and different mesh refinement levels are highlighted. Furthermore, it is possible to evaluate the mesh compliance with the packing geometry.

Model equations and simulation set-up

In all simulations, we considered the case of an isothermal turbulent flow of a Newtonian fluid at steady state. The fluid was considered incompressible because the flow Mach number, i.e. the ratio of the flow velocity to the velocity of sound in the fluid was well below 0.1 for all the tested situations. All properties of the fluid were considered constant across the whole computational domain. For the purposes of this investigation, we used the simpleFoam solver from the OpenFOAM toolbox. The simpleFoam is a steady state solver that uses the SIMPLE algorithm[26,27] to compute the pressure-velocity coupling.

Governing equations

A stationary isothermic turbulent flow of an incompressible Newtonian fluid is described by the set of Navier-Stokes equations in the form

$$\begin{aligned} \nabla \cdot (\boldsymbol{u} \otimes \boldsymbol{u}) - \nabla \cdot \boldsymbol{\tau} &= -\nabla p \\ \nabla \cdot \boldsymbol{u} &= 0\,, \end{aligned} \tag{1}$$

where $\boldsymbol{u}$ corresponds to the velocity field, p to the kinematic pressure and $\boldsymbol{\tau}$ to the viscous stress tensor defined as $\boldsymbol{\tau} = \nu \nabla \boldsymbol{u}$. The coefficient ν denotes the fluid kinematic viscosity. In both experiments and simulations, we are interested purely in the pressure loss due to energy dissipation and we neglect the hydrostatic pressure. Thus, gravity is omitted in equations (1).

To take into account the effects of turbulence without having to resolve a transient

problem with numerous length scales, we applied the Reynolds averaged form of the Navier-Stokes equations (RANS),

$$\begin{aligned} \nabla \cdot (\overline{\boldsymbol{u}} \otimes \overline{\boldsymbol{u}}) - \nabla \cdot (\overline{\boldsymbol{\tau}} + \boldsymbol{\tau}') &= -\nabla \overline{p} \\ \nabla \cdot \overline{\boldsymbol{u}} &= 0\,, \end{aligned} \tag{2}$$

where $\overline{\boldsymbol{u}}$ and $\overline{p}$ are the averaged velocity and pressure, respectively. The new variable $\boldsymbol{\tau}'$, is the so called Reynolds stress tensor in the form $\boldsymbol{\tau}' = \boldsymbol{u}' \otimes \boldsymbol{u}'$ and $\boldsymbol{u}'$ is the instantaneous turbulence driven velocity fluctuation.

Because of the presence of the non-linear Reynolds stress term $\nabla \cdot \boldsymbol{\tau}'$, the formulation (2) requires additional modeling to be closed. In the present work, we select the Menter's $k-\omega$ shear stress transport (SST) model[28] in the formulation given by Hellsten[29] as the most suitable approach for the closure of the problem (2). In the following, we work solely with the averaged variables and the over-lines in the symbols notation are omitted.

Boundary conditions and initial guess

The system (2) needs to be completed with suitable boundary conditions. Let $\mathcal{S} \subset \mathbb{R}^3$ be the computational domain corresponding to the packed column inside. We denote the boundary of $\mathcal{S}$ as $\partial\mathcal{S}$ and divide it into three different subdomains,

$$\partial\mathcal{S} = \partial\mathcal{S}_{\text{inlet}} \cup \partial\mathcal{S}_{\text{outlet}} \cup \partial\mathcal{S}_{\text{wall}}\,. \tag{3}$$

Because the complete specification of the boundary conditions is given in Table 3, only a few explanatory notes will be given in the following text.

At the inlet, we prescribed Dirichlet boundary conditions for the velocity $\boldsymbol{u}$, turbulence kinetic energy k, and the specific dissipation rate ω. Although it would be possible to prescribe more complex and physical inlet boundary conditions, based on the work of Khosravi-Nikou and Eshani[22] and our own tests, we concluded that the error caused directly by the used

Table 3: Applied boundary conditions. The column height and diameter are denoted as h_{col} and r_{col}, respectively. The column height corresponds to the height of the packed bed extended symmetrically by 3 cm long inlet and outlet empty pipe sections. Symbol $\mathbf{n}_f$ denotes the outer unit normal to the boundary and B is the representation of the packed bed defined by Algorithm 1.

Boundary	Conditions
$\partial\mathcal{S}_{\mathrm{inlet}} = \left\{\boldsymbol{x} = (x, y, z) \in \mathbb{R}^3 : x = -\frac{h_{\mathrm{col}}}{2}, y^2 + z^2 \leq r_{\mathrm{col}}^2\right\}$	$\boldsymbol{u} = (u_i, 0, 0)^{\mathrm{T}}$ $\mathbf{n}_f \cdot \nabla p = 0$ $k = k_0$ $\omega = \omega_0$
$\partial\mathcal{S}_{\mathrm{outlet}} = \left\{\boldsymbol{x} \in \mathbb{R}^3 : x = \frac{h_{\mathrm{col}}}{2}, y^2 + z^2 \leq r_{\mathrm{col}}^2\right\}$	$\mathbf{n}_f \cdot \nabla \boldsymbol{u} = (0, 0, 0)^{\mathrm{T}}$ if $\boldsymbol{\Phi} > 0$, $\boldsymbol{u} = (0, 0, 0)^{\mathrm{T}}$ else $p = 0$ $\mathbf{n}_f \cdot \nabla k = 0$ if $\boldsymbol{\Phi} > 0$, $k = k_0$ else $\mathbf{n}_f \cdot \nabla \omega = 0$ if $\boldsymbol{\Phi} > 0$, $\omega = \omega_0$ else $\boldsymbol{\Phi} = \mathbf{n}_f \cdot \boldsymbol{u}$
$\partial\mathcal{S}_{\mathrm{wall}} = B \cup \left\{\boldsymbol{x} \in \mathbb{R}^3 : x = \left\langle -\frac{h_{\mathrm{col}}}{2}, \frac{h_{\mathrm{col}}}{2} \right\rangle, y^2 + z^2 = r_{\mathrm{col}}^2\right\}$	$\boldsymbol{u} = (0, 0, 0)^{\mathrm{T}}$ $\mathbf{n}_f \cdot \nabla p = 0$ $\mathbf{n}_f \cdot \nabla k = 0$ $\mathbf{n}_f \cdot \nabla \omega = 0$

boundary conditions is negligible.

At the outlet, we specified an inlet-outlet boundary conditions for $\boldsymbol{u}$, k and ω. The inlet-outlet boundary condition prescribes a zero-gradient Neumann type boundary condition for the case of the fluid outflow defined as $\boldsymbol{\Phi} = \mathbf{n}_f \cdot \boldsymbol{u} > 0$, where $\mathbf{n}_f$ is the outer unit normal to the boundary. Otherwise, a Dirichlet type boundary condition is prescribed. Furthermore, we fixed the pressure at the outlet by a Dirichlet type boundary condition.

On the walls, which consist of the column hull and the packing itself, we prescribed a standard no-slip boundary condition for the velocity and the zero-gradient boundary condition for the pressure. Furthermore, the mesh was refined in the way, that the nearest cells to the wall boundaries lie within the flow laminar sublayer. Hence, we did not need to apply any special wall functions to the turbulence variables k and ω.

The problem specification was completed by the prescribed initial guess,

$$\boldsymbol{u}^{(0)} = (0, 0, 0)^{\mathrm{T}}, \quad p^{(0)} = 0, \quad k^{(0)} = k_0, \quad \omega^{(0)} = \omega_0, \quad \forall \boldsymbol{x} \in \mathcal{S}\,, \tag{4}$$

where the initial guesses for k and ω were estimated via the following relations,

$$\begin{aligned} k_0 &= \frac{3}{2}\left(u_f I_0\right)^2, \quad I_0 = 0.0853 Re^{-0.0727}, \\ Re &= \frac{u_f d_h}{\nu}, \quad u_f = \frac{u_i}{\varepsilon_{\mathrm{pk}} \sin \alpha_{\mathrm{ch}}}, \\ \omega_0 &= \frac{\epsilon_0}{k_0}, \quad \epsilon_0 = \frac{0.1643 k_0^{3/2}}{0.07 d_h}. \end{aligned} \tag{5}$$

In the above equations, u_f denotes an estimate of the mean free stream velocity in a packing channel calculated from the gas inlet velocity u_i, the structured packing porosity $\varepsilon_{\mathrm{pk}}$, and the channel inclination angle α_{ch}. The symbol I_0 stands for the turbulence intensity and it is approximated using the formula of Russo and Basse[30] for the flow in a smooth pipe, which is based on the flow Reynolds number Re. The used Reynolds number is evaluated from the estimate for the free stream velocity in the channels u_f, the channels hydraulic diameter d_h, and the fluid kinematic viscosity ν.

Results and Discussion

In this section, we first present results of the mesh independence study performed to determine how fine a grid is required to capture the important flow physics. Then, we will proceed to the model validation, which is done through a comparison of measured and calculated dry pressure losses. The dry pressure loss is a difference between the pressures above and below the packed bed relative to the height of the packed bed,

$$\Delta p_h := \frac{p_{\mathrm{above}} - p_{\mathrm{below}}}{N_{\mathrm{pk}} H_{\mathrm{pk}}}, \tag{6}$$

where H_{pk} is the height of a single packing element and N_{pk} is the number of packing elements present in the packed bed.

After the model validation and a discussion of the minimum number of packing elements necessary to predict Δp_h of the whole packed bed, we estimate the dependence of Δp_h on

the channel inclination angle α_{ch}, packing geometric area density a_{G}, and on the distance between the centers of two adjacent holes of packing perforation a_{pr}.

Mesh size independence

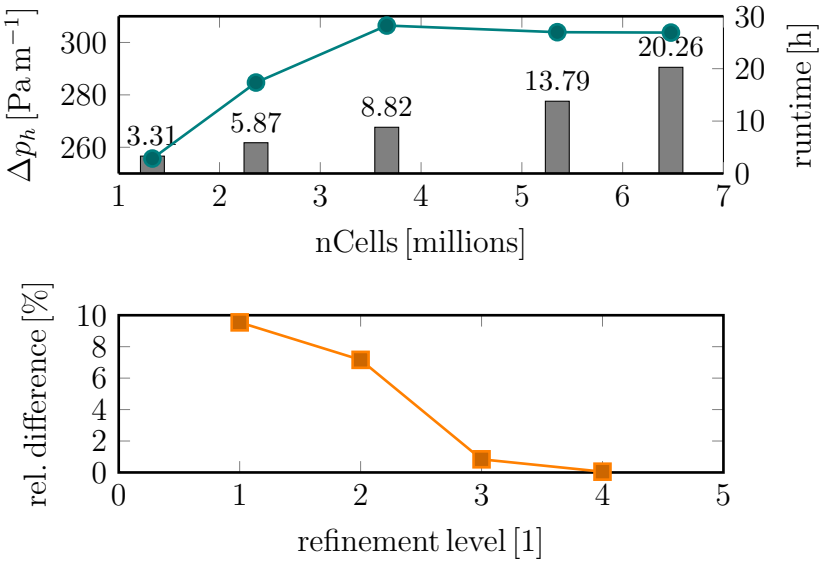

Figure 3: Mesh size independence study. The tests were performed for the N_2 gas, $u_i = 3.05\,\mathrm{m\,s^{-1}}$, and one element of the Mellapak 250.Y packing. The relative error between two consecutive mesh refinement levels was computed as $|\Delta p_h^{\ell+1} - \Delta p_h^{\ell}|/\Delta p_h^{\ell+1} \cdot 100\,\%$, where ℓ is the mesh refinement level.

The calculated dry pressure loss for the selected mesh sizes as well as the simulations runtimes on 4 cores of the Altix UV2000 commercial cluster[31] are depicted in the top part of Figure 3. At the beginning, the calculated pressure loss increased with the mesh refinement. However, with the number of cells in the mesh around $4 \cdot 10^6$, the computed dry pressure loss stabilized. More specifically, the difference between the Δp_h calculated on the mesh with approximately $5.3 \cdot 10^6$ cells per one packing element and the Δp_h calculated on the mesh with approximately $6.4 \cdot 10^6$ cells per packing element was less then 0.5 %. Hence, for the calculations, we used the meshes with the size corresponding to $5.3 \cdot 10^6$ cells per one packing element.

The mesh size independence study was performed using the model of packing corre-

sponding to the Mellapak 250.Y. The meshes applied for simulations of flow in packings with different geometric area densities were generated using the same snappyHexMesh settings and inputs. Thus, the mesh sizes in these simulations ranged from $5.3 \cdot 10^6$ cells per packing element for Mellapak 250.Y to $8.3 \cdot 10^6$ cells per packing element for Mellapak 500.Y.

Model validation

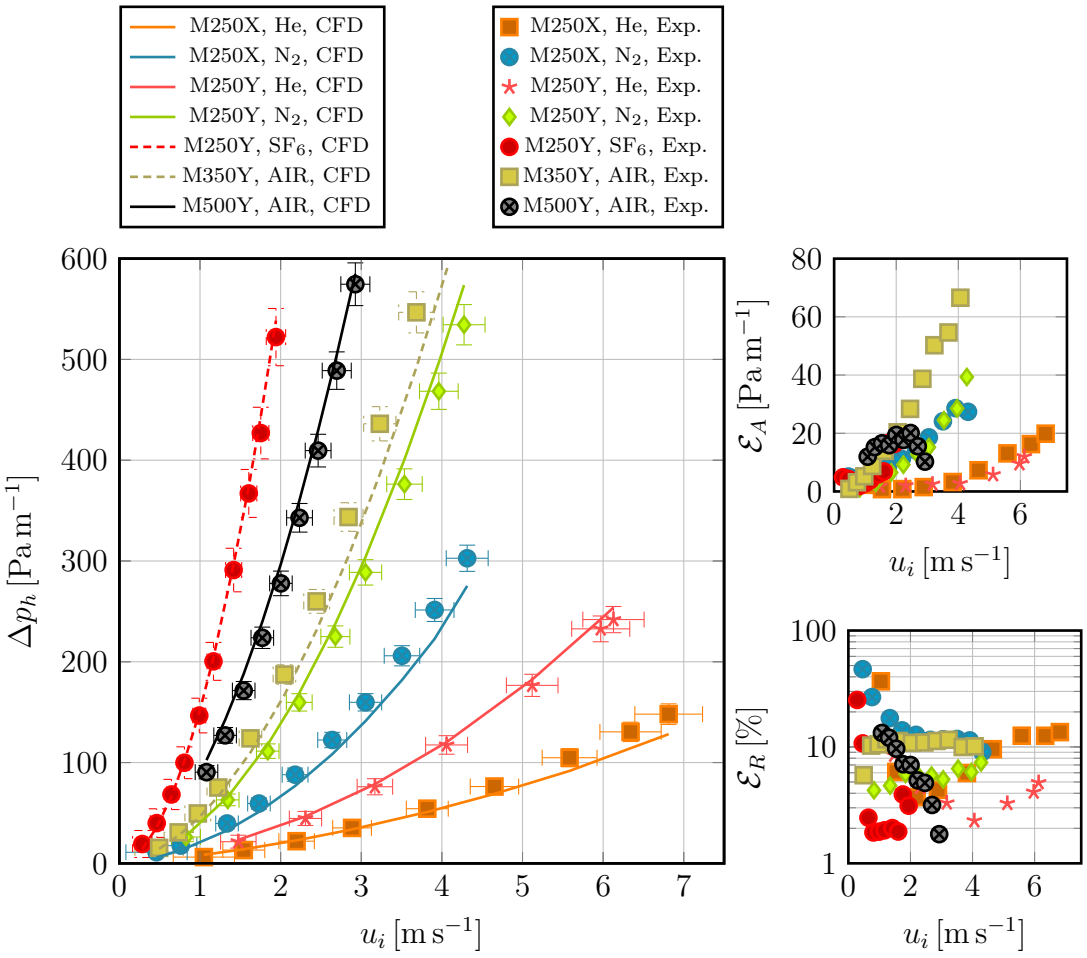

Figure 4: Results of the model validation obtained on one packing element. In the left part of the figure, there are directly compared measured and calculated dry pressure losses. The included horizontal and vertical error bars correspond to $2\sigma_{u_i}$ and $2\sigma_{\Delta p_h}$, respectively. In the top right subplot, we depict the absolute differences between the experiment and CFD. In the bottom right subplot, the corresponding relative differences are shown.

The model validation was done on the experimental data measured as described in Sec. "Experimental". The model geometry was designed to match the experimental set

up as much as possible. The only difference was the lack of wall wipers in the model geometry. The fluid properties of the individual gases were fixed to the values given in Table 2. In Figure 4, we compare the measured and calculated Δp_h for all the available data.

For all the used packings and experimental conditions, the relative difference between the measured and estimated values,

$$\mathcal{E}_R := \frac{\left|\Delta p_h^{\text{Exp.}} - \Delta p_h^{\text{CFD}}\right|}{\Delta p_h^{\text{Exp.}}} \cdot 100\ \%\,, \tag{7}$$

was usually around or below 10 %. The only exceptions were the measurements with extremely low gas flow rates, where the $\mathcal{E}_R$ might go up to 30 %. On the other hand, as the $\Delta p_h^{\text{Exp.}}$ was close to the lowest measurable value, the experimental data in these cases could be burdened with some error. All the Δp_h calculated using CFD fall within the range of extended uncertainties of the experimental data.

Effect of packed bed length on the dry pressure loss

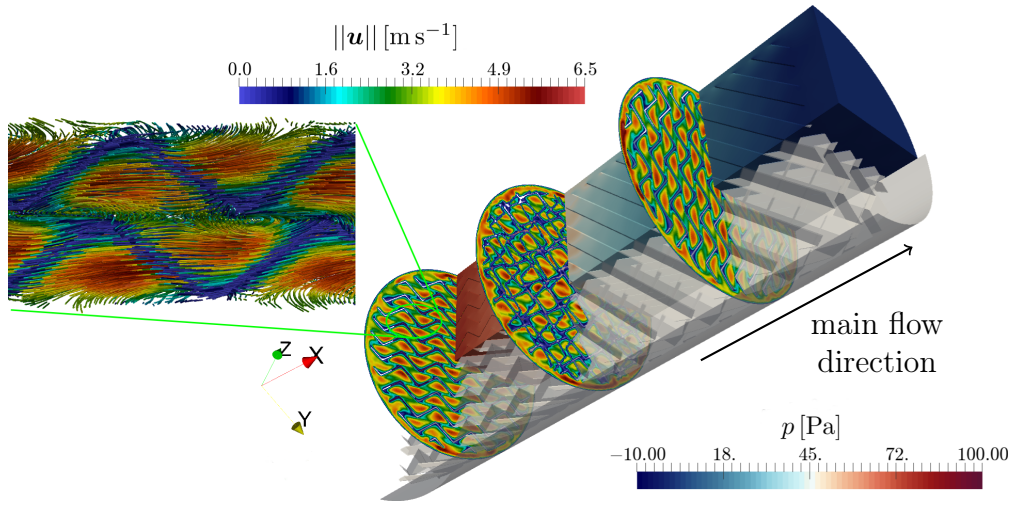

Figure 5: Pressure and velocity fields in two elements of Mellapak 250.Y. The velocity field is depicted on three different slices, two of which are in the middle of the individual packing elements and one is located directly at the contact of the two elements. A detailed view of the streamlines near the contact of two packing channels is shown on the left hand side of the figure. (He, $u_i = 2.3\,\mathrm{m\,s^{-1}}$)

In Figure 5, we show a typical result for the simulation of flow in two packing elements. The change in the pressure field along the column is mostly monotone and smooth. The depicted velocity field suggests a formation of regular flow patterns in each of the considered packing elements. Furthermore, upon inspection of the detailed view of the streamlines near the contact of two packing channels, see Figure 5, it can be stated that there is almost no mixing at the contact of adjacent sheets within one packing element. In other words, with respect to the limitations of the used Reynolds averaging, the gas flowing inside one channel does not seem to be mixed with the gas flowing in the adjacent channels oriented in the opposite direction.

To evaluate the effect of the length of the packed bed on the dry pressure loss, it is necessary to compare the pressure field in the individual packing elements. The flow at the contact of two packing elements, see the middle slice in Figure 5, is perturbed because the gas is forced to change its flow direction. Such a steep change of the flow direction is connected with a significant energy dissipation. Remarkably, the comparison of the pressure loss computed on one and two packing elements, see Figure 6-(a), suggests that a single packing element is sufficient to estimate the dry pressure loss of the whole packed bed.

To analyze the effect of the transition between two packing elements on the overall pressure loss, we studied the evolution of the slice-averaged normalized pressure,

$$\left(\overline{p}(x_i)\right)_n = \frac{1}{\max\limits_{\boldsymbol{x}\in\mathcal{S}} p}\left(\frac{1}{\eta^{y-z}(x_i)}\int_{\eta^{y-z}(x_i)} p\,\mathrm{d}S\right), \quad \eta^{y-z}(x_x) = \{\boldsymbol{x}\in\mathcal{S} : x = x_i\}\ , \tag{8}$$

along a packed bed consisting of two packing elements. In Figure 6-(b), we show the evolution of $(\overline{p})_n$ along a column filled with two packing elements rotated by 90 degrees with respect to each other. The used packings correspond to M250X and M250Y. Three different situations are depicted for each packing, (i) flow in the laminar regime, which corresponds to the flow of helium at $u_i = 1.05\,\mathrm{m\,s^{-1}}$ and $Re \approx 130$, (ii) flow in the transition regime, which corresponds to the flow of nitrogen at $u_i = 3.05\,\mathrm{m\,s^{-1}}$ and $Re \approx 2500$, and (iii) flow in the

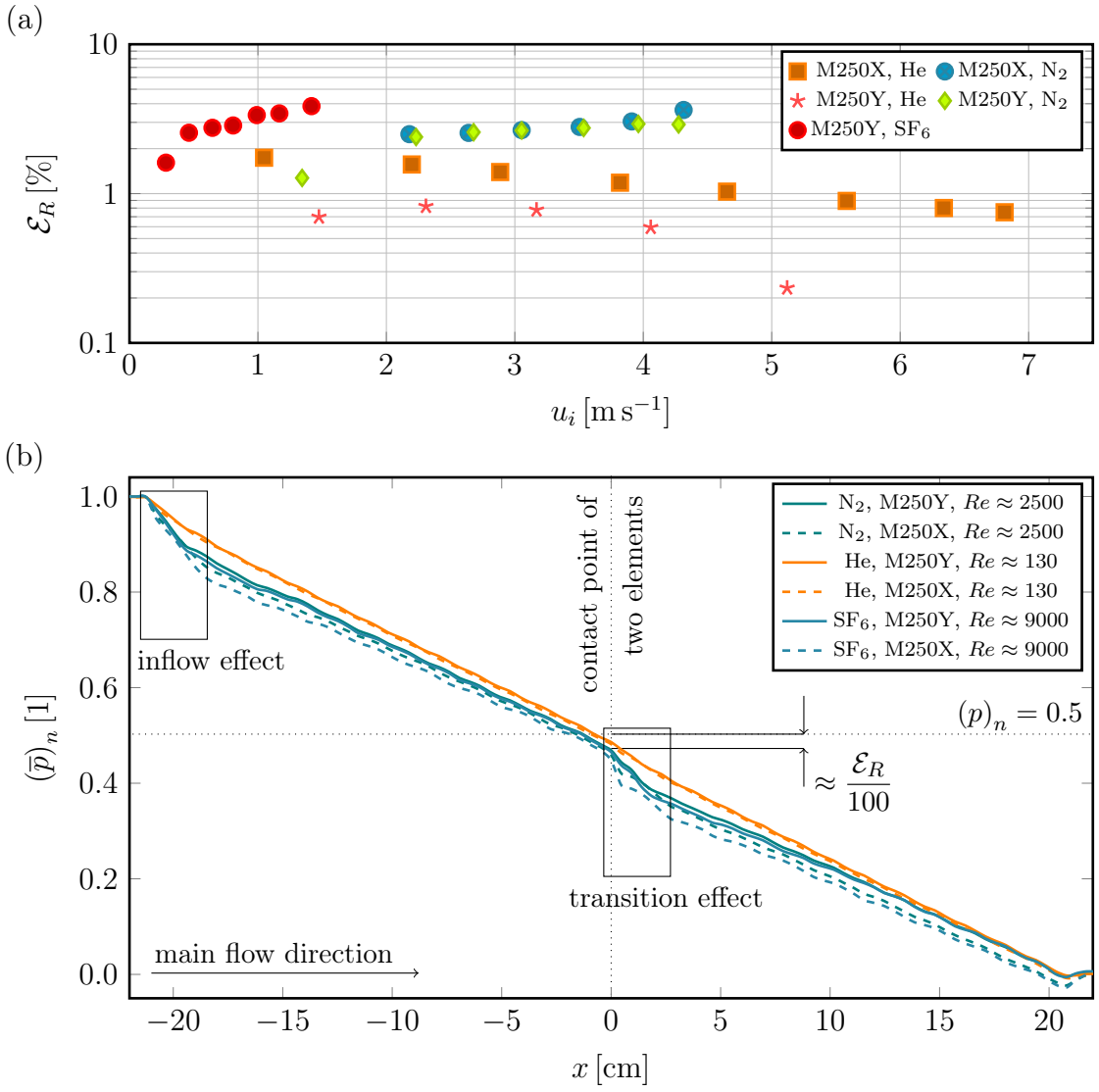

Figure 6: (a) Comparison of the relative difference between the calculated Δp_h for one and two packing elements. The relative error was computed as $|\Delta p_h^{2\,\mathrm{p.e.}} - \Delta p_h^{1\,\mathrm{p.e.}}|/\Delta p_h^{2\,\mathrm{p.e.}} \cdot 100\,\%$. (b) Evolution of slice-averaged normalized pressure along a column with internal diameter of 15 cm filled with two packing elements. Error caused by performing the computations on a single packing element is highlighted.

turbulent regime, which corresponds to the flow of sulfur hexafluoride at $u_i = 1.94\,\mathrm{m\,s^{-1}}$ and $Re \approx 9000$.

From the results depicted in Figure 6-(b), it can be estimated that the transition effect between two packing elements accounts for $15 - 20\%$ of the pressure loss on the individual elements in mostly and completely turbulent flow regimes (N_2 and SF_6 data) and for less than 5% in the mostly laminar flow regime (He data). It can also be seen that the transition effect is, with respect to the total pressure loss, more significant for X-type packing than for the Y-type. These results are in a perfect agreement with the Delft Model[32,33] and findings of Larachi et al.[21], which are both based on the analysis of individual contributions of different packing geometry elements to the overall pressure loss. However, the results shown in Figure 6-(b) reveal a significant inflow effect in the bed entrance region. In fact, our simulations suggest that the impact of the inflow effect on the evolution of $(\overline{p})_n$ is comparable to the transition effect, i.e. the pressure loss due to the single flow direction change at the entrance to the packed bed is of the same magnitude as the pressure loss due to the transition between two packing elements. This finding is inconsistent with the conclusions of Larachi et al.[21], who reported almost one order of magnitude higher pressure loss due to the transition effect than to the inflow effect. Nevertheless, the similarity between the inflow and the transition effects explains the small differences in the pressure loss calculated on one and two packing elements, see Fig.6-(a).

To further examine the similarity between the pressure profiles in the first and the following packing elements, i.e. the similarity between the inflow effect and the transition effect, a simulation of N_2 at $u_i = 3.05\,\mathrm{m\,s^{-1}}$ on six elements of M250Y packing was performed. In Figure 7-(a), we show the dry pressure loss of each packing element relative to one sixth of the dry pressure loss of the whole packed bed. The biggest relative error (5.2%) was encountered for the packing element number six, i.e. for the outflow element of the packed bed. In Figure 7-(b), we compare the normalized averaged pressure profiles in the individual packing elements. The differences between the respective profiles are, from the qualitative point of

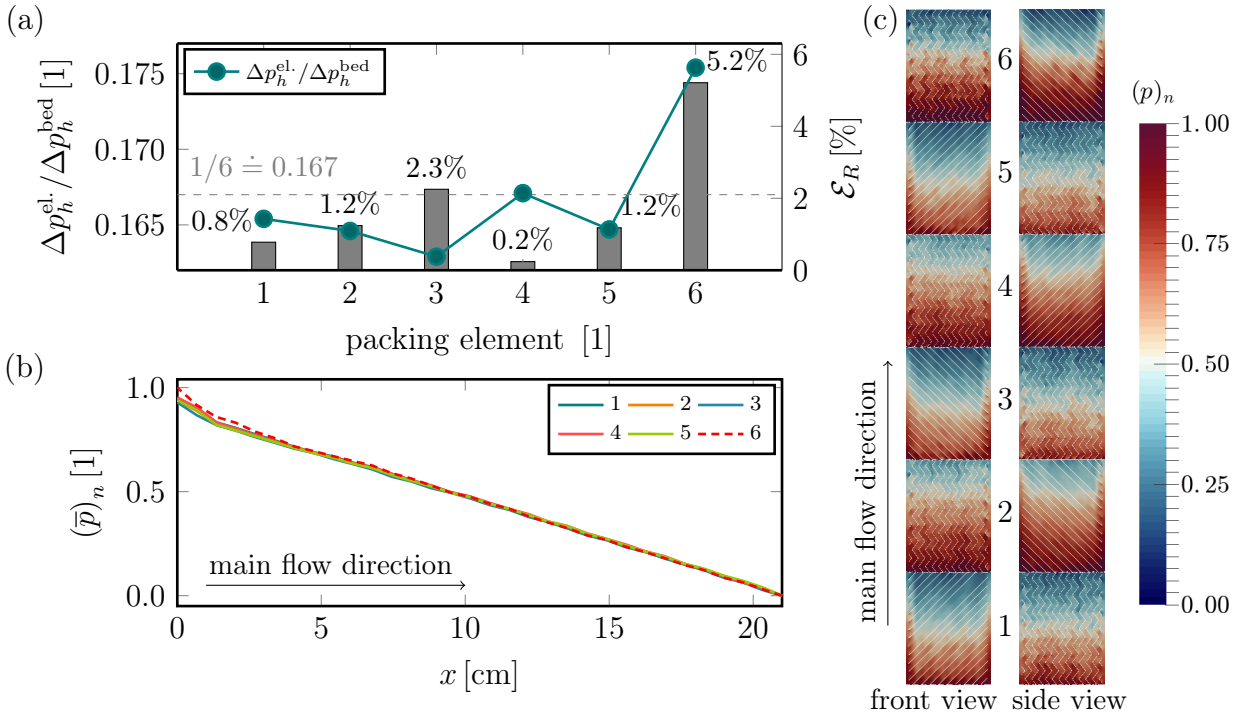

Figure 7: Pressure distribution in a column of i.d. of 15 cm filled with six M250Y packing elements. (N_2, $u_i = 3.05\,\mathrm{m\,s^{-1}}$, $Re \approx 2500$) (a) Contribution of each of the six packing elements to the overall pressure loss on the packed bed. (b) Evolution of the normalized slice-averaged pressure along different packing elements. (c) Normalized pressure distribution on slices made through the middle of the column.

view, negligible. Moreover, the normalized pressure distribution appears to be almost the same in all the six packing elements, see Figure 7-(c).

Dry pressure loss estimation

The final part of this study is devoted to the estimation of the packing dry pressure loss based on the packing geometrical parameters, namely the inclination of the channels to the horizontal α_{ch}, the density of the packing geometric area a_{G}, and the density of the perforation expressed through the distance between the adjacent centers of the perforation holes in y axis direction a_{pr}^{Y}. The distance between the holes centers in the x direction is kept constant at $a_{\mathrm{pr}}^{X} = 0.05\,\mathrm{m}$.

We are interested mostly in the qualitative behavior of the studied packing geometries. Thus, we define a normalized dry pressure loss as

$$(\Delta p_h)_n^i := \frac{\Delta p_h^i}{\max_{(i)} \Delta p_h}\,, \tag{9}$$

where we denoted the current value by the superscript i and all the available values of interest as (i). The definition of $(\Delta p_h)_n$ enables us to compare the trends in the dry pressure loss evolution for different systems.

From the above presented results, we selected three reference conditions for which we studied the development of the dry pressure loss. The selected systems were the same as in the previous section, i.e. the flow of He at $u_i = 1.05\,\mathrm{m\,s^{-1}}$ and Re in M250Y ≈ 130, the flow of N_2 at $u_i = 3.05\,\mathrm{m\,s^{-1}}$ and $Re \approx 2500$ and the flow of SF_6 at $u_i = 1.94\,\mathrm{m\,s^{-1}}$ and $Re \approx 9000$. Such systems were chosen because they represent the variety in both the channel flow Reynolds numbers and the velocities at the geometry inlet.

First, we were interested in the dependence of $(\Delta p_h)_n$ on the channel inclination to the horizontal α_{ch}. We created a series of different packings geometries with α_{ch} varying from 0° to 90° and with the geometric area density of $a_{\mathrm{G}} = 250\,\mathrm{m^2 m^{-3}}$. Examples of the compared

geometries are depicted in borders of Figure 8. For each packing geometry and each of the reference conditions, we performed a CFD simulation of flow in one packing element and computed Δp_h.

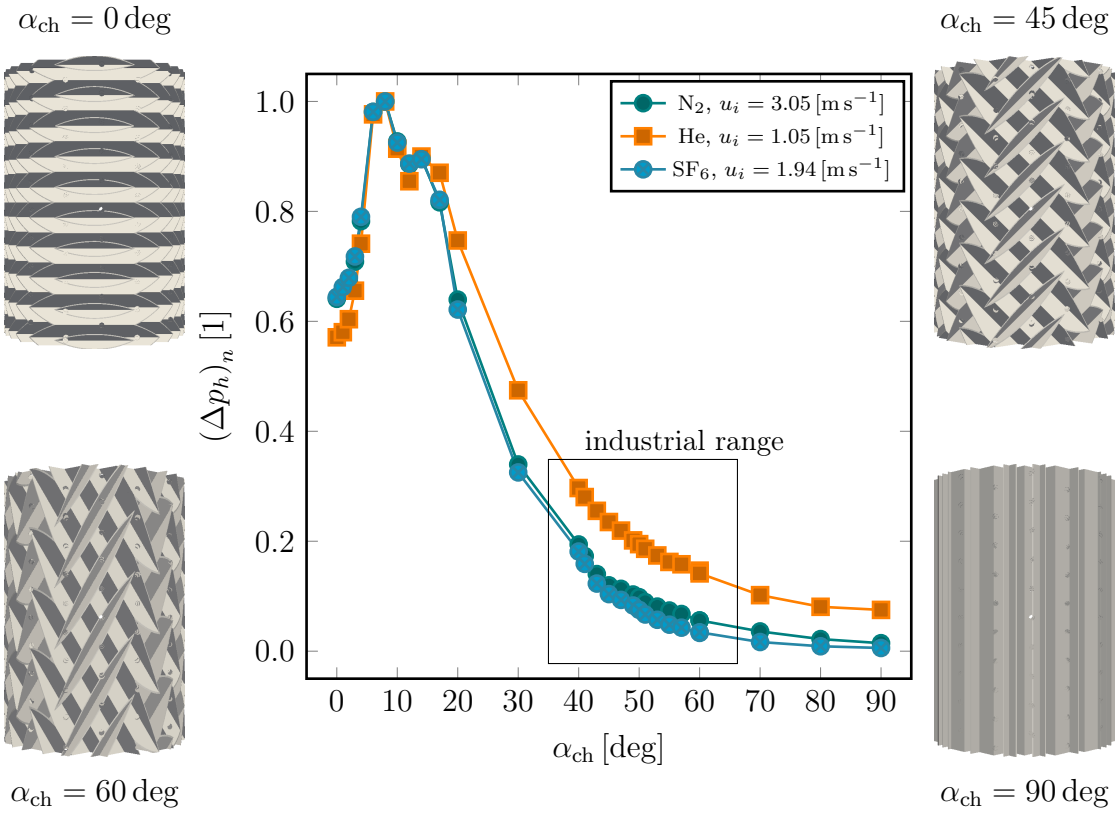

Figure 8: Dependence of the normalized dry pressure loss on the channel inclination angle. Data calculated on one packing element with $a_G = 250\,m^2m^{-3}$ are shown. Emphasis was made on channel inclinations of interest for the industry and on channel inclinations lower than 20°, for which the depicted curve shows a counter-intuitive trend.

The obtained results are depicted in Figure 8. For $\alpha_{ch} > 20°$, the overall trend is as expected, i.e. with the increase in α_{ch} the dry pressure loss decreases rather sharply for all the tested combinations of the gas properties and inlet velocity. The predicted data follow the dependence of $\Delta p_h \propto \sin^{-3} \alpha_{ch}$, which can be derived if the packing is modeled as a bundle of inclined triangular tubes.[32,33] The absolute values of minimal and maximal measured Δp_h significantly varied between the test cases and are given in Table 4.

All the studied systems exhibited a maximum in $(\Delta p_h)_n$ for $\alpha_{ch} \approx 8°$. The presence of such a maximum seems counter-intuitive. Nevertheless, we believe that it may be explained

Table 4: Overview of the minimal and maximal absolute values of Δp_h obtained for different packing geometries.

Case	Varied parameter	$\min \Delta p_h\,[\mathrm{Pa\,m^{-1}}]$	$\max \Delta p_h\,[\mathrm{Pa\,m^{-1}}]$
N_2	α_{ch}	36.9	2540
He	α_{ch}	4.61	61.4
SF_6	α_{ch}	30.2	5190
N_2	a_{G}	303	611
He	a_{G}	14.4	41.3
SF_6	a_{G}	538	1010
N_2	a_{pr}^{Y}	254	323
He	a_{pr}^{Y}	13.1	14.7
SF_6	a_{pr}^{Y}	462	604

via investigation of the flow field in the packing channels. In Figure 9-(a), (b) and (c), we show detailed views of the streamlines of He, $u_i = 1.05\,\mathrm{m\,s^{-1}}$ in geometries corresponding to $\alpha_{\mathrm{ch}} = \{0, 8, 20\}^\circ$, respectively. Streamlines in the mid-section of the packing element are depicted in the top part of each sub-figure. In the bottom, we present typical flow patterns across the column in the direction consistent with the channels orientation.

If the channels are perpendicular to the main flow direction, i.e. for $\alpha_{\mathrm{ch}} = 0^\circ$, the gas crosses the channels, but it is not forced to flow along them. In the bottom part of Figure 9-(a), it may be seen that the streamlines are, especially in the column center, almost parallel one to another. On the column sides, the flow in the packing is affected by the gas flowing in the gap between the packing and the column hull. The only observed irregularity in the flow was encountered in the vicinity of the perforation, see the slowly moving gas in the middle of the bottom part of Figure 9-(a).

As the channel inclination angle increases, the gas starts to flow along the channels and destabilizes the flow pattern, formed for $\alpha_{\mathrm{ch}} = 0^\circ$. The increasing flow instability is associated with the sharp increase in the dry pressure loss for $\alpha_{\mathrm{ch}} \in (0, 6)^\circ$ visible in Figure 8. For $\alpha_{\mathrm{ch}} \in (6, 20)^\circ$, the amount of gas flowing along and across the channels is comparable and

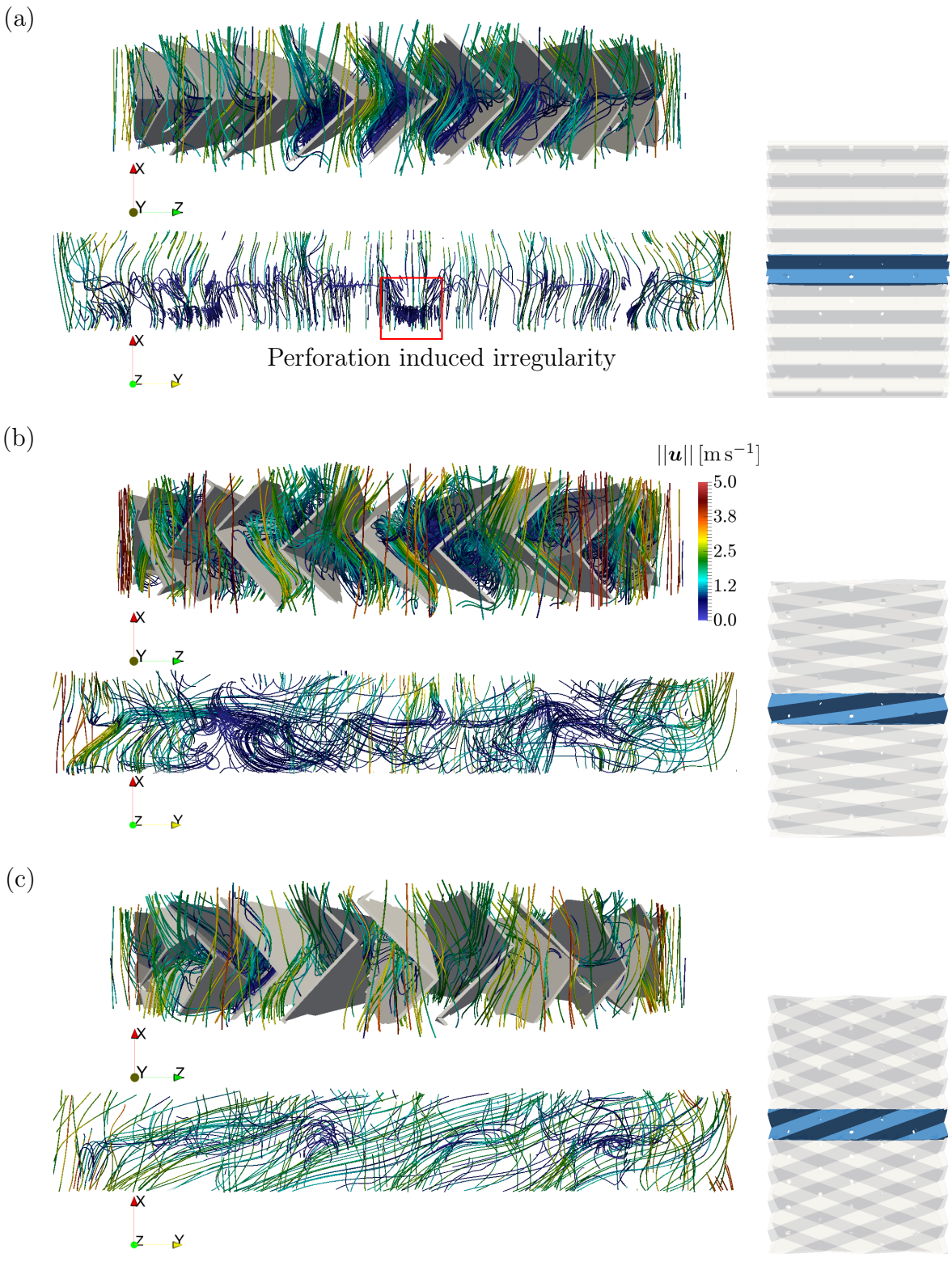

Figure 9: Streamlines in selected parts of the geometry. (a) $\alpha_{\mathrm{ch}} = 0°$, (b) $\alpha_{\mathrm{ch}} = 8°$, (c) $\alpha_{\mathrm{ch}} = 20°$. The middle part of a packing element is shown on top and flow patterns across the column in the direction of the channels are shown in bottom. (He, $u_i = 1.05\,\mathrm{m\,s^{-1}}$)

the flow is chaotic, consult Figure 9-(b). If the channel inclination angle is increased above $\alpha_{\mathrm{ch}} \approx 20°$, the majority of the gas starts to flow along the channels and a new stable flow pattern, visible in Figure 9-(c) and Figure 5, emerges.

Second, we investigated the dependence of the packing dry pressure loss on the packing geometric area density a_{G}. We generated a series of geometries with the geometric area density ranging from $a_{\mathrm{G}} = 250\,\mathrm{m}^2\,\mathrm{m}^{-3}$ to $a_{\mathrm{G}} = 500\,\mathrm{m}^2\,\mathrm{m}^{-3}$. The packing with the lowest and highest geometric area corresponded to the Mellapak 250.Y and Mellapak 500.Y, respectively. Examples of different generated packings are given in borders of Figure 10.

The packing parameters modified to vary its geometric area density were the length of the packing channel side a_{ch} and the length of the hypotenuse of the triangle formed by the channel sides s_{ch}. These parameters were adjusted as

$$\left.\begin{array}{rcl} a_{\mathrm{ch}} & = & \varpi a_{\mathrm{ch}}^{\mathrm{M500}} + (1-\varpi) a_{\mathrm{ch}}^{\mathrm{M250}} \\ s_{\mathrm{ch}} & = & \varpi s_{\mathrm{ch}}^{\mathrm{M500}} + (1-\varpi) s_{\mathrm{ch}}^{\mathrm{M250}} \end{array}\right. , \quad \varpi \in \langle 0, 1 \rangle \,, \tag{10}$$

where the superscripts M500 and M250 denote the dimensions of Mellapak 500.Y and 250.Y, respectively. Note that the channel dimensions corresponding to the Mellapak 350.Y cannot be exactly reconstructed from the convex combination (10) of the dimensions of Mellapak 500.Y and Mellapak 250.Y. Nevertheless, the error in the Mellapak 350.Y channel dimensions is less then 3 % and the obtained geometric area density is exactly the same.

The dependence of the normalized dry pressure loss on the packing geometric area density is shown in Figure 10. Interestingly, the dry pressure loss estimated for the system corresponding to the flow of helium at low velocities increased more than three times between M250Y and M500Y whilst the dry pressure loss computed for the flow of sulfur hexafluoride at relatively high inlet velocity changed in the same situation approximately two times.

We offer an explanation for the encountered behavior from the point of view of the flow regime. For $a_{\mathrm{G}} \gtrapprox 450\,\mathrm{m}^2\mathrm{m}^{-3}$ all three simulated cases follow approximately the same trend.

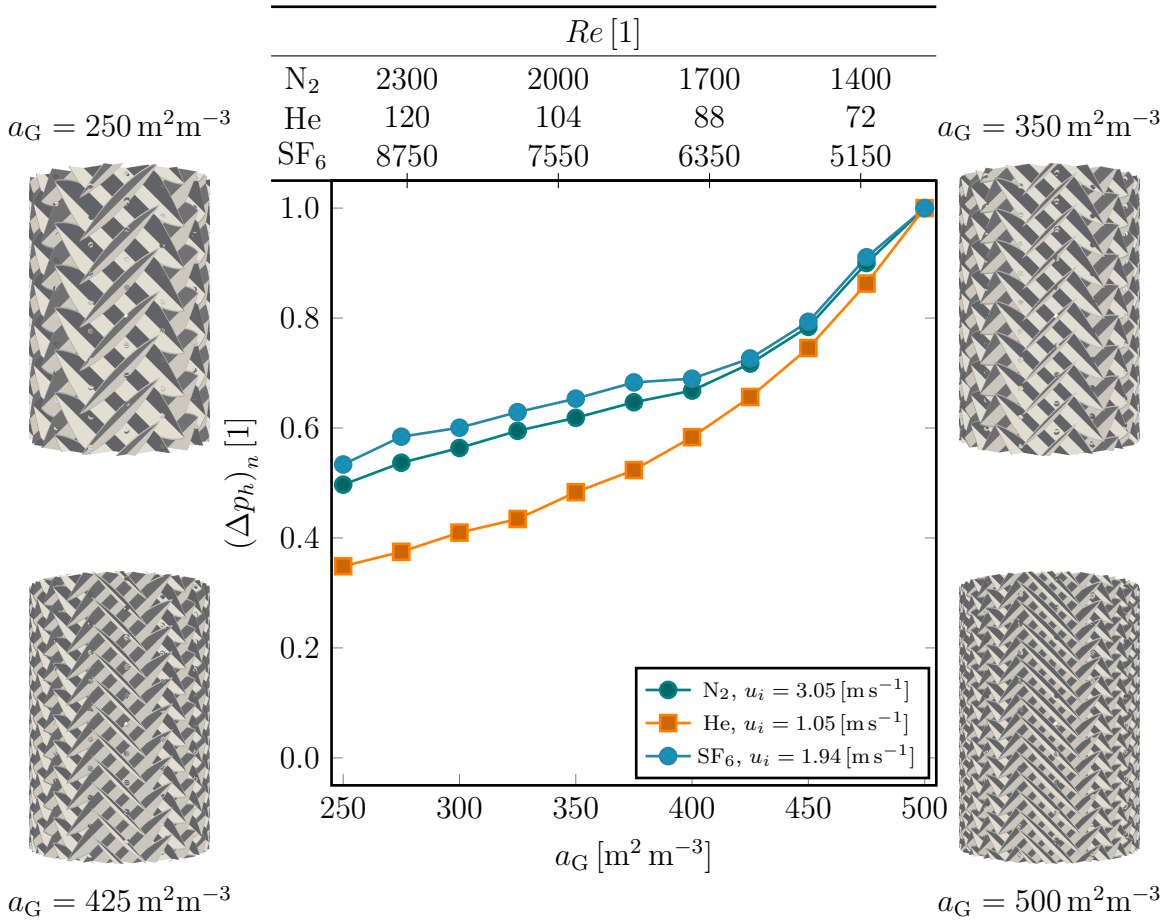

Figure 10: Dependence of the normalized dry pressure loss on the packing geometric area density a_G, for Mellapak type Y packing. Flow Reynolds numbers are shown on an auxiliary x axis. Examples of packings with different a_G are shown in image borders.

Then, for $a_{\mathrm{G}} \in (400, 450)\,\mathrm{m^2 m^{-3}}$ the dependence of the normalized dry pressure loss on a_{G} for the flow of helium at low speed separates from the remaining two curves. Finally, for $a_{\mathrm{G}} \lessapprox 350\,\mathrm{m^2 m^{-3}}$ all the three dependencies are distinct.

For high packing geometric area densities, the channels are narrow and even the flow of SF_6 at $u_i = 1.94\,\mathrm{m\,s^{-1}}$ is close to the laminar regime. With decreasing a_{G}, the channels in packing become more and more open and the effects of turbulence accentuate.

The flow of helium at $u_i = 1.05\,\mathrm{m\,s^{-1}}$ remains close to the laminar regime for all the tested packing geometric area densities. On the other hand, for the case of N_2 and especially for SF_6 the turbulence develops in channels of packings with $a_{\mathrm{G}} \lessapprox 450\,\mathrm{m^2 m^{-3}}$. The development of turbulence causes the aforementioned change in the trend of the dependence of $(\Delta p_h)_n$ on a_{G}.

The last parameter of interest was the packing perforation density, which we expressed through the distance between the two adjacent perforation holes centers in y axis direction, a^Y_{pr}. Amongst the commercial packings, the perforation density is one of the most varied parameters and ranges from no perforation at all to highly perforated packings with a_{pr} well below 0.01 m. Surprisingly the perforation holes diameter D_{pr}, is almost always close to 5 mm.

In Figure 11, we depict the dependence of $(\Delta p_h)_n$ on a^Y_{pr} for the three studied reference conditions. As an auxiliary horizontal axis, we include the number of perforation holes in the y axis direction. To normalize the computed dry pressure loss, we did not use the maximal computed dry pressure loss. Instead the pressure loss of an unperforated packing was applied as the scale.

The dependence of $(\Delta p_h)_n$ on a^Y_{pr} is not monotone and the highest dry pressure loss was not obtained for the unperforated packing. The oscillations in the data seem to depend not only on the density of the perforation but also on the actual position of the perforation holes. For example, for SF_6 and $a^Y_{\mathrm{pr}} \in (6.5, 11.0)\,\mathrm{cm}$ the dry pressure loss oscillates approximately between 95% and 105% of the dry pressure loss of an unperforated packing. In this case,

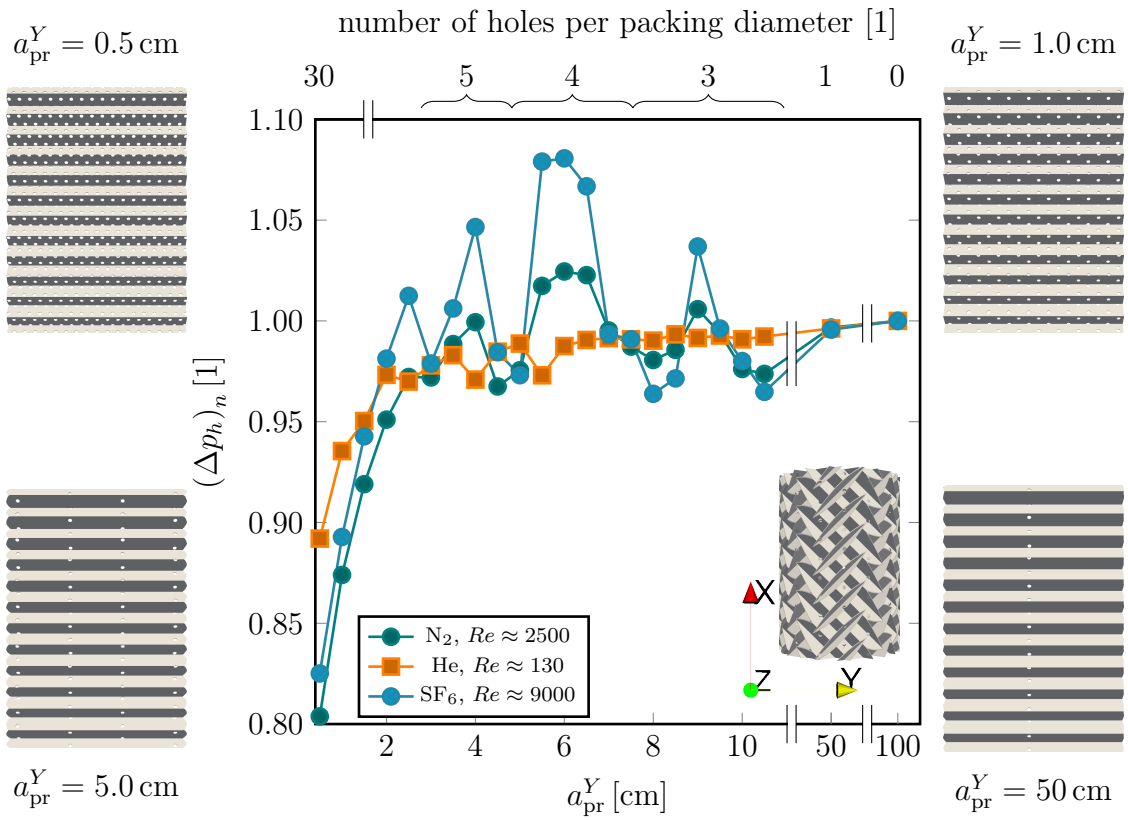

Figure 11: Dependence of the normalized dry pressure loss on the packing perforation density expressed through the distance between two adjacent cell centers in the y direction, a^Y_{pr}. Results for three different channel Reynolds numbers are depicted. Corrugated sheets of dimensions $21 \times 15\,\mathrm{cm}$ with different perforation densities are shown in image borders. ($\alpha_{\mathrm{ch}} = 45\,\mathrm{deg}$, $a_{\mathrm{G}} = 250\,\mathrm{m^2 m^{-3}}$)

the number of holes per packing diameter remains the same: 3. The position of the holes is changed in a way that one set of holes is fixed in the center of the packing, similarly as it is depicted in the bottom right corner of Figure 11, and two sets of holes are placed symmetrically at $a^Y_{\mathrm{pr}}/2$ from the packing center. Hence, with increasing a^Y_{pr}, the side holes move towards the packing margins and the only thing altering the flow inside the packing is the change in position of these side holes. A similar, albeit less pronounced, trend was observed for nitrogen as well.

Our theory is that the change of position of the perforation connected with even a slight change in the perforation density may influence the structure of the flow perturbations induced by the presence of the perforation. The perforation-induced flow perturbations cause energy dissipation in the system and as such they increase the system pressure loss. Olujic et al.[34] distinguishes between dissipation mechanisms that contribute to the packing mass transfer efficiency and the ones that do not. Unfortunately, in which group belongs the perforation-induced dissipation remains, up to our knowledge, an open question.

Regardless of the effects of the perforation on the flow structure, the perforation opens new paths for the gas. Our simulations imply that the packings with $a^Y_{\mathrm{pr}} < 2\,\mathrm{cm}$, i.e. with 7 or more holes per the packing diameter (14 cm), exhibit a significantly lower dry pressure loss than the unperforated packings. The results on the left-hand side of Figure 11 show that for helium, increasing the number of perforation holes from 7 to 15 and from 15 to 30 causes a decrease in the dry pressure loss of approximately 5%, each; compare the fourth to second and the second to first data point from the left. For nitrogen and sulfur hexafluoride, the respective decreases in pressure loss are between 7% and 9%.

Finally, note that the observed effect of the perforation density is relevant only for the dry packing. In the case of a wet packing, it can be expected that a considerable part of the perforation holes will be covered by the liquid film. Consequently, the effects of perforation on the packing pressure loss may change or even be eliminated.

Conclusions

Nowadays, the distillation is the most energy-intensive technology of the chemical industry. Nevertheless, the design of the distillation columns remains mostly empirical. In an attempt to shed some light on the intricacies of the gas flow in the widely used type of commercial packings, the structured packing consisting of corrugated sheets, we provided a relatively quick and accurate method to generate a geometric representation of these packings. Furthermore, we constructed a CFD model for the gas flow through the structured packing. We validated the model on custom-measured experimental data and used it to study the flow characteristics in the Mellapak type structured packings. An emphasis was made on the similarity between the gas inflow and transition effects in the packed bed and on the implications of this similarity on the minimal number of packing elements necessary to predict the dry pressure loss of the whole packed bed. Finally, the developed methods were combined to estimate the dry pressure loss of the Mellapak type structured packing in dependence on the channel inclination angle, packing geometric area density, and the perforation density of the corrugated sheets. It was shown, that the channel inclination and the packing geometric area density play a significantly more important role from the point of view of the packing dry pressure loss than the packing perforation. However, highly perforated packings have noticeably lower dry pressure loss than the unperforated ones. In the future research, we would like to focus on the modeling of the multiphase flow in the Mellapak type packings as well as on the development of the models for the flow in other types of widely used separation columns internals, including random packings.

Acknowledgement

This work was supported by the Centre of Excellence for nonlinear dynamic behaviour of advanced materials in engineering CZ.02.1.01/0.0/0.0/15_003/0000493 (Excellent Research Teams) in the framework of Operational Programme Research, Development and Education.

References

(1) Ozokwelu, D. *Distillation column modeling tools*; 2001; p 2.

(2) Demirel, Y. Sustainable operations for distillation columns. *Chem. Eng. Process Tech.* **2013**, *1*, 15.

(3) Bertoldi, P.; Lorente, J. L.; Labanca, N. *Energy consumtion and energy efficiency trends in the EU-28 2000-2014*; 2016; p 238.

(4) Green, D.; Perry, R. *Perry's Chemical Engineers' Handbook*, 8th ed.; McGraw Hill professional; McGraw-Hill Education: New York, 2007.

(5) Seader, J. D.; Henley, E. J. *Separation process principles*, 2nd ed.; Wiley & Sons: Hoboken, NJ, 2005.

(6) SET-Plan Secreatariat, *Continue efforts to make EU industry less energy intensive and more competitive*; 2016; p 13.

(7) Haroun, Y.; Raynal, L. Use of computational fluid dynamics for absorption packed column design. *Oil Gas Sc. Technol.* **2015**, *71*, 1–18.

(8) Owens, S. A.; Perkins, M. R.; Eldridge, R. B.; Schulz, K. W.; Ketcham, R. A. Computational fluid dynamics simulation of structured packing. *Ind. Eng. Chem. Res.* **2013**, *52*, 2032–2045.

(9) Amini, Y.; Karimi-Sabet, J.; Esfahany, M. N. Experimental and numerical simulation of dry pressure drop in high-capacity structured packings. *Chem. Eng. Technol.* **2016**, *39*, 1161–1170.

(10) Fernandes, J.; Simoes, P. C.; Mota, J. P. B.; Saatdjian, E. Applications of CFD in the study of supercritical fluid extraction with structured packing: Dry pressure drop calculations. *J. of Supercritical Fluids* **2008**, *47*, 17–24.

(11) Fernandes, J.; Lisboa, P. F.; Simoes, P. C.; Mota, J. P. B.; Saatdjian, E. Applications of CFD in the study of supercritical fluid extraction with structured packing: Wet pressure drop calculations. *J. of Supercritical Fluids* **2009**, *50*, 61–68.

(12) Raynal, L.; Royon-Lebeaud, A. A Multi-Scale Approach For CFD Calculations of Gas-Liquid Flow Within Large Size Column Equipped With Structured Packing. *Chem. Eng. Sci.* **2007**, *62*, 7196–7204.

(13) Cooke, J. J.; Gu, S.; Armstrong, L. M.; Luo, K. H. Gas-Liquid Flow on Smooth and Textured Inclined Planes. *World. Ac. of Sc., Eng. and Technol.* **2012**, *68*, 1712–1719.

(14) Hoffmann, A.; Ausner, I.; Repke, J.-U.; Wozny, G. Detailed Investigation of Multiphase (Gas-Liquid and Gas-Liquid-Liquid) Flow Behaviour on Inclined Plates. *Chem. Eng. Res. and Des.* **2006**, *84*, 147–154.

(15) Saleh, A. R.; Hosseini, S. H.; Shojaee, S.; Ahmadi, G. CFD studies of pressure drop and increasing capacity in MellapakPlus 752.Y structured packing. *Chem. Eng. Technol.* **2011**, *34*, 1402–1412.

(16) Xu, Y.; Yuan, J.; Repke, J.-U.; Wozny, G. CFD Study on Liquid Flow Behavior on Flat Plate Focusing on Effect of Flow Rate. *Eng. Appl. of Comp. Fluid Mech.* **2012**, *6*, 186–194.

(17) Haroun, Y.; Raynal, L.; Alix, P. Prediction of Effective Area and Liquid Hold-up in Structured Packings by CFD. *Chem. Eng. Res. and Des.* **2014**, *92*, 2247–2254.

(18) Sebastia-Saez, D.; Gu, S.; Ranganathan, P. 3D Modeling of Hydrodynamics and Physical Mass Transfer Characteristics of Liquid Flom Flows in Structured Packing Elements. *Int. J. of Greenhouse Gas Cont.* **2013**, *19*, 492–502.

(19) Zhang, Y.-L.; Zhu, H.-M.; Yin, Q.-X. CFD study on the local mass transfer efficiency in the gas phase of structured packing. *Chem. Eng. Technol.* **2013**, *36*, 1138–1146.

(20) Sebastia-Saez, D.; Gu, S.; Ranganathan, P.; Papadikis, K. Micro-scale CFD Study About the Influence of Operative Parameters on Physical Mass Transfer Within Structured Packing Elements. *Int. J. of Greenhouse Gas Cont.* **2014**, *28*, 180–188.

(21) Larachi, F.; Petre, C. F.; Iliuta, I.; Grandjean, B. Tailoring the pressure drop of structured packings throught CFD simulations. *Chem. Eng. Proc.* **2003**, *42*, 535–541.

(22) Khosravi-Nikou, M. R.; Eshani, M. R. Turbulence models application on CFD simulation of hydrodynamics, heat and mass transfer in a structured packing. *Int. Comm. Heat Mass Tr.* **2008**, *17*, 21.

(23) Blender Online Community, Blender – a 3D modelling and rendering package. Blender Foundation: Amsterdam, 2016.

(24) OpenCFD, *OpenFOAM: The Open Source CFD Toolbox. User Guide*; OpenCFD Ltd: Reading, UK, 2016.

(25) SGI Apps Engineering, *OpenFOAM 4.0: The SGI MotorBike Standard Benchmark*; 2016; p 4.

(26) Ferziger, J. H.; Peric, M. *Computational methods for fluid dynamics*, 3rd ed.; Springer-Verlag: Berlin, 2002.

(27) Moukalled, F.; Darwish, M.; Mangani, L. *The finite volume method in computational fluid dynamics: an advanced introduction with OpenFOAM and Matlab*, 1st ed.; Springer-Verlag: Berlin, 2016.

(28) Menter, F. R. *Improved two equation k-ω turbulence models for aerodynamic flows*; 1992; p 34.

(29) Hellsten, A. Some improvements in Menter's k-ω SST turbulence model. Proceedings of the Fluid Dynamics Conference. 1997; p 11.

(30) Russo, F.; Basse, N. T. Scaling of turbulence intensity for low-speed flow in smooth pipes. *Flow Meas. Inst.* **2016**, *52*, 101–114.

(31) SGI Gobal Sales and Support, *SGI UV 2000: Data sheet*; 2015; p 2.

(32) Olujic, Z. Effect of column diameter on pressure drop of a corrugated sheet structured packing. *Trans. IChemE (A)* **1999**, *77*, 505–510.

(33) Dejanovic, I.; Matijasevic, L.; Jansen, H.; Olujic, Z. Designing a packed dividing wall column for an aromatics processing plant. *Ind. Eng. Chem. Res.* **2011**, *50*, 5680–5692.

(34) Olujic, Z.; Jansen, H.; Kaibel, B.; Rietfort, T.; Zich, E. Stretching the capacity of structured packings. *Ind. Eng. Chem. Res.* **2001**, *40*, 6172–6180.

Geometry generation procedure

The process of the geometry creation leverages the regularity of the Mellapak type packing structure. More specifically, the packing is formed by a series of channels with a triangular cross-section as it is shown in Figure 1-(e). Thus the geometry of the Mellapak type packing can be described using only several different parameters, namely the dimensions of one channel, the channel side length a_{ch}, and the angle between the channel sides θ_{ch}, the number of channels appertaining to one corrugated metal sheet, N_{ch}, the channel inclination to the horizontal α_{ch}, the number of metal sheets to be created, N_{sh} and the overall size of the packing described by its diameter and height, D_{pk} and H_{pk}, respectively. Furthermore, we describe the packing perforation by the diameter of one hole D_{pr}, and the distance between the centers of two adjacent holes a_{pr}. Finally, the whole packing bed might be defined by the number of the packing elements N_{pk}, and the respective rotation of the two adjacent packing elements φ_{pk}. The last parameter required for the geometry creation is the thickness of the used metal sheets. This parameter was fixed at $w_{\mathrm{sh}} = 0.5\,\mathrm{mm}$ as finner sheets caused instabilities during the meshing process.

The geometry generation process is specified in Algorithm 1. For the clarity of the notation, we use a combination of a global Cartesian coordinate system (O, x, y, z) with a local coordinate systems $(\tilde{O}_i, \tilde{x}_i, \tilde{y}_i, \tilde{z}_i)$. The center of the local coordinate system $\tilde{O}_i$, is fixed at the centroid of the object i and the local axis $(\tilde{x}_i, \tilde{y}_i, \tilde{z}_i)$ are parallel with the global ones (x, y, z).

Algorithm 1 Mellapak type geometry creation

Require: Packing geometry parameters: $a_{\mathrm{ch}}, \theta_{\mathrm{ch}}, N_{\mathrm{ch}}, \alpha_{\mathrm{ch}}, N_{\mathrm{sh}}, D_{\mathrm{pk}}, H_{\mathrm{pk}}, D_{\mathrm{pr}}, a_{\mathrm{pr}}, N_{\mathrm{pk}}, \varphi_{\mathrm{pk}}, w_{\mathrm{sh}}$

Create the first channel side, s_1, of dimensions $a_{\mathrm{ch}} \times 2D_{\mathrm{pk}}/\sin\alpha_{ch} \times w_{\mathrm{sh}}$ at position $\boldsymbol{x}_{s_1} = ((a_{\mathrm{ch}} - w_{\mathrm{sh}})\cos\theta_{\mathrm{ch}}, 0, 0)^{\mathrm{T}}$;
Rotate s_1 by $\theta_{\mathrm{ch}}/2$ along the $\tilde{y}_{s_1}$ axis;
for $i = 2$ **to** $2N_{\mathrm{ch}}$ **do**
    Duplicate the previous channel side, $s_i \leftarrow s_{i-1}$;
    Update the location of s_i, $\boldsymbol{x}_{s_i} = (i(a_{\mathrm{ch}} - w_{\mathrm{sh}})\cos\theta_{\mathrm{ch}}, 0, 0)^{\mathrm{T}}$;
    Rotate s_i by $(i \mod 2)\theta_{\mathrm{ch}}$ along the $\tilde{y}_{s_i}$ axis;
end for
Join all the channel sides to one corrugated sheet, $S_1 := \bigcup_{i=1}^{2N_{\mathrm{ch}}} s_i$;
Update the position of the global coordinate system, $(O, x, y, z) := (\tilde{O}_{S_1}, \tilde{x}_{S_1}, \tilde{y}_{S_1}, \tilde{z}_{S_1})$;
Rotate S_1 by $-\alpha_{\mathrm{ch}}$ along the $\tilde{z}_{S_1}$ axis;
for $i = 2$ **to** N_{sh} **do**
    Duplicate the previous sheet, $S_i \leftarrow S_{i-1}$;
    Update the location of S_i, $\boldsymbol{x}_{S_i} = (0, 0, (i - \mathrm{floor}\,(N_{\mathrm{sh}}/2))a_{\mathrm{ch}}\sin\theta_{\mathrm{ch}})^{\mathrm{T}}$;
    Rotate S_i by $(-1)^i\alpha_{\mathrm{ch}}$ along the $\tilde{z}_{S_i}$ axis;
end for
Join all the sheets to one packing element, $P_1 := \bigcup_{i=1}^{N_{\mathrm{sh}}} S_i$;
Update the position of the global coordinate system, $(O, x, y, z) := (\tilde{O}_{P_1}, \tilde{x}_{P_1}, \tilde{y}_{P_1}, \tilde{z}_{P_1})$;
Cut out the cylindrical shape of the packing, $P_1 := \{(x, y, z) \in P_1 : y^2 + z^2 \leq D_{\mathrm{pk}}^2/4 \wedge |x| \leq H_{\mathrm{pk}}/2\}$
Create the perforation, $P_1 := P_1 \backslash \{(x, y, z) \in P_1 : (x - ia_{\mathrm{pr}})^2 + (y - ja_{\mathrm{pr}})^2 \leq D_{\mathrm{pr}}^2/4\}_{i,j\in\mathbb{Z}}$;
for $i = 2$ **to** N_{pk} **do**
    Duplicate the previous packing element, $P_i \leftarrow P_{i-1}$;
    Update the location of P_i, $\boldsymbol{x}_{P_i} = ((1/2 + i - 2)H_{\mathrm{pk}}, 0, 0)^{\mathrm{T}}$;
    Rotate P_i by $(i \mod 2)\varphi_{\mathrm{pk}}$ along the $\tilde{x}_{P_i}$ axis;
end for
Join all the packing elements to a packed bed, $B := \bigcup_{i=1}^{N_{\mathrm{pk}}} P_i$;
Update the position of the global coordinate system, $(O, x, y, z) := (\tilde{O}_B, \tilde{x}_B, \tilde{y}_B, \tilde{z}_B)$;
return Geometry representation of the packed bed suitable for the snappyHexMesh utility

Using the Algorithm 1, it is possible to create a usable geometry for the Mellapak type packing within minutes. Because also the rest of the modeling process can be fully auto-

mated, it is possible to study the dependence of the flow behavior on the geometry parameters. Furthermore, additional features, such as the collars (or wall wipers) visible on the left side of Figure 1-(d) can be easily added to the geometry.

Graphical TOC Entry

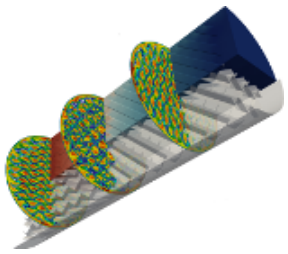

Velocity and pressure fields in structured packing.